Quantum phase diagram of the spin-1 J_1-J_2 Heisenberg model on the honeycomb lattice

Shou-Shu Gong, Wei Zhu, and D. N. Sheng

Department of Physics and Astronomy, California State University, Northridge, California 91330, USA

Strongly correlated systems with geometric frustrations can host the emergent phases of matter with unconventional properties. Here, we study the spin $S = 1$ Heisenberg model on the honeycomb lattice with the antiferromagnetic first- (J_1) and second-neighbor (J_2) interactions ($0.0 \leqslant J_2/J_1 \leqslant 0.5$) by means of density-matrix renormalization group. In the parameter regime $J_2/J_1 \lesssim 0.27$, the system sustains a Néel antiferromagnetic phase. At the large J_2 side $J_2/J_1 \gtrsim 0.32$, a stripe antiferromagnetic phase is found. Between the two magnetic ordered phases $0.27 \lesssim J_2/J_1 \lesssim 0.32$, we find a *nonmagnetic* intermediate region with a plaquette valence-bond order. Although our calculations are limited within a six unit-cell width on cylinder, we present evidence that this plaquette state could be a strong candidate for this nonmagnetic region in the thermodynamic limit. We also briefly discuss the nature of the quantum phase transitions in the system. We gain further insight into the nonmagnetic phases in the spin-1 system by comparing its phase diagram with the spin-1/2 system.

I. INTRODUCTION

Since Anderson proposed the resonating valence bond theory to explain high-temperature superconductivity [1], the study of spin liquid (SL) [2–11] in frustrated magnetic systems has been attracting much attention for almost 40 years [12,13]. In recent years, this field has achieved exciting progress with identifying realistic examples of SL states. Among the various SL candidates, the most promising candidate is the spin-1/2 kagome antiferromagnet. On the experimental side, strong evidence supporting the gapless SL has been discovered in the spin-1/2 kagome antiferromagnet materials herbertsmithite [14–17] and kapellasite [18–21]. In theoretical studies, the spin-1/2 kagome Heisenberg model has been found to sustain a SL ground state although the nature of the SL is still under debate between the gapped Z_2 SL [22–25] obtained from density-matrix renormalization group (DMRG) and the gapless $U(1)$ Dirac SL favored in the variational studies of the Gutzwiller projected wave function [26–28]. Very recently, by introducing the second- and third-neighbor interactions [29–31] or the chiral interactions [32] in kagome systems, a gapped chiral spin liquid which breaks time-reversal symmetry is unambiguously established as the $\nu = 1/2$ fractional quantum Hall state through fully characterizing the topological properties [30–32] of the state.

Besides the kagome systems, the spin-1/2 J_1-J_2 Heisenberg models on the square and honeycomb lattices have also been considered as promising candidates of SL. In particular, the SL on square lattice is considered significant to understand the high-temperature superconductivity in copper oxide [1]. Recently, the long-debated nonmagnetic regions in these two models have been studied intensively as possible realizations of gapped Z_2 SL [33–36] or gapless SL [37,38]. By performing DMRG calculations on cylinder systems [39–42], it is found that the Z_2 SL behaviors in the intermediate region of both models appear not stable on the wide systems. Instead, a plaquette valence-bond (PVB) state may dominate the nonmagnetic regions.

The frustrated spin-1 magnetic systems on the square and honeycomb lattices are also particularly interesting as they

may be the parent magnetic systems for the iron-based superconductivity. The square Heisenberg models with frustrating further-neighbor couplings and quadratic interactions [43–48] have been studied intensively using the mean-field analysis to investigate the possible nematic order. By using DMRG calculations on the spin-1 J_1-J_2 square Heisenberg model [46], a nonmagnetic phase between the Néel and the stripe antiferromagnetic (AFM) phase is obtained. However, the nature of this nonmagnetic phase is far from clear although a nematic paramagnetic state has been proposed based on the field-theory description [49]. On the other hand, the frustrated spin-1 honeycomb Heisenberg models have not been studied systematically, which may be relevant to the spin model for the honeycomb iron-based superconductivity material SrPtAs [50–54]. For the spin-1/2 J_1-J_2 honeycomb model [33,39–41,55–68], a Néel AFM phase and a staggered dimer phase are found at $J_2 \lesssim 0.22$ and $J_2 \gtrsim 0.35$, respectively. Between these two phases for $0.25 \lesssim J_2 \lesssim 0.35$, a PVB phase is identified in DMRG calculations [39–41] as the PVB correlation length keeps growing fast with system width on cylinder [40,41]. For the spin $S = 1$ J_1-J_2 model, the studies are rare and it is unclear whether the quantum phases such as the PVB and the staggered dimer phases would persist with spin magnitude increasing from 1/2 to 1, and what kinds of classical states might emerge in the honeycomb system [69].

In this paper, we study the spin-1 Heisenberg model on the honeycomb lattice with the frustrating J_1-J_2 AFM interactions by using the DMRG with spin rotational $SU(2)$ symmetry [70,71]. The Hamiltonian of the model is given as

$$H = J_1 \sum_{\langle i,j \rangle} \mathbf{S}_i \cdot \mathbf{S}_j + J_2 \sum_{\langle\langle i,j \rangle\rangle} \mathbf{S}_i \cdot \mathbf{S}_j, \tag{1}$$

where J_1 and J_2 are the first- and second-neighbor AFM interactions. We set J_1 as the energy scale, and lattice spacing between the nearest-neighbor sites as the length scale. Through our $SU(2)$ DMRG calculations on cylinder systems, we establish a quantum phase diagram as shown in Fig. 1. By studying the spin correlation function, we find a Néel AFM phase for $0 \leqslant J_2 \lesssim 0.27$. For $0.5 \geqslant J_2 \gtrsim 0.32$, we find the
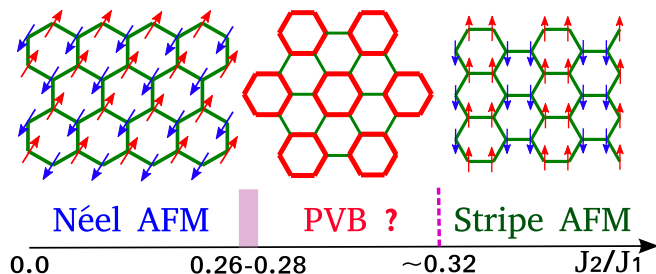
FIG. 1. (Color online) Quantum phase diagram of the spin-1 J_1-J_2 Heisenberg model on the honeycomb lattice. With increasing J_2 coupling, the system has a Néel AFM phase for $J_2 < 0.26$, a stripe AFM phase for $J_2 \gtrsim 0.32$, and an intermediate non-magnetic phase with a plaquette valence-bond order in our DMRG calculations. As the finite-size effects on different cylinder geometries, the first transition point is estimated at $0.26 \sim 0.28$.

magnetic ordered state rather than the staggered dimer state. In this region, the obtained magnetic order state depends on the cylinder geometry in our finite-size calculations. By comparing the ground-state bulk energy on different cylinder geometries, we find that the stripe AFM state always possesses the lower energy and thus appears to be the ground state in the thermodynamic limit. Between the two magnetic order phases $0.27 \lesssim J_2 \lesssim 0.32$, the system has a narrow nonmagnetic region with nonuniform bond energy on wide cylinders. During the increase of the kept states from 2000 to 8000 $SU(2)$ states, a PVB dimer order is found stabilized on the studied cylinder systems, which suggests that the PVB state is a strong candidate for this intermediate phase region. Finally, we discuss the nature of the quantum phase transitions in the system with the help of the bipartite entanglement entropy.

In our DMRG calculations, we study the cylinder systems with widths up to 8 (6) unit cells in the magnetic ordered phases (intermediate phase), by keeping up to 8000 $SU(2)$ states to ensure the convergence. The truncation error is controlled below 10^{-6} for the $L_y = 4$ (L_y is the number of unit cells in the y direction) cylinder and below 10^{-5} for the other calculations. The cylinder geometries are shown in Fig. 2. The first cylinder ACm-n has the armchair open edges, where m is the number of two-site unit cells along the y direction and n is the number of columns along the x direction. The second cylinder has the zigzag open edges and is denoted as the ZCm-n cylinder.
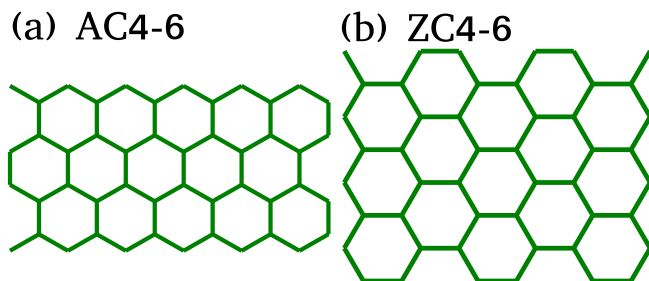

FIG. 2. (Color online) Cylinder geometries used in the DMRG calculations. (a) is an AC4-6 cylinder and (b) is a ZC4-6 cylinder.

II. NÉEL AFM PHASE

First of all, we study the Néel AFM phase in the small J_2 side. Due to the limit of system width in the DMRG calculations for the spin-1 system, we do not have enough data of magnetization on different system widths to estimate the result in thermodynamic limit through extrapolation. Instead, on the finite-width cylinders, we calculate the spin correlation functions along the cylinder axis direction (the x direction) and study their decay behaviors with increasing J_2.

In Fig. 3, we demonstrate the spin correlation functions in real space for $J_2 = 0.0$ on the AC4-24 and ZC4-24 cylinders. Clearly, the spin correlations exhibit a Néel AFM pattern with two magnetic sublattices. We follow the J_2 dependence of the spin correlation decaying to detect the vanishing of Néel order. On the AC4-24 cylinder in Fig. 4(a), we find that the spin correlation length keeps decreasing with growing J_2, which reaches a minimum at $J_2 \simeq 0.25$. Slightly above $J_2 = 0.25$, such as $J_2 = 0.27$ as shown in Fig. 4(a), the Néel AFM pattern of correlations is destructed, which signals a phase transition with vanishing the Néel order. On the ZC4-24 cylinder as shown in Fig. 4(b), we find that the spin correlations decay much slower than those on the AC4-24 cylinder near the transition point, which indicates the finite-size effects of the system when approching phase boundary. Beyond $J_2 \sim 0.28$, the spin correlations decay fast as shown in Fig. 4(b) at $J_2 = 0.29$. Based on the spin correlations on both AC4 and ZC4 cylinders, we estimate the Néel order vanishing at $J_2 \sim 0.26$–0.28.

Based on the decay behaviors of spin correlations, we plot the J_2 dependence of the long-distance spin correlations $S_d \equiv \sqrt{|\langle S_0 S_d \rangle|}$ [d is the longest distance in Figs. 4(a) and 4(b)] as shown in Figs. 4(c) and 4(d). We find that the vanishing of S_d and the destruction of the Néel AFM pattern on both geometries are consistent with a phase transition at
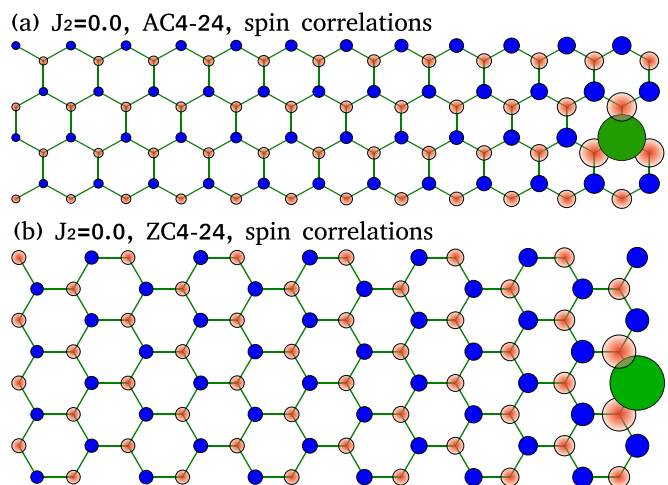
(a) J$_2$=0.0, AC4-24, spin correlations

(b) J$_2$=0.0, ZC4-24, spin correlations

FIG. 3. (Color online) Spin correlation functions in real space for $J_2 = 0.0$ on the (a) AC4-24 cylinder and (b) ZC4-24 cylinder. The green site is the reference site in the middle of the cylinder, and the blue solid and red shaded circles denote the positive and negative correlations, respectively. The radius of the circle is proportional to the magnitude of correlations. Here, we only show the left half $2 \times 4 \times 12$ sites.
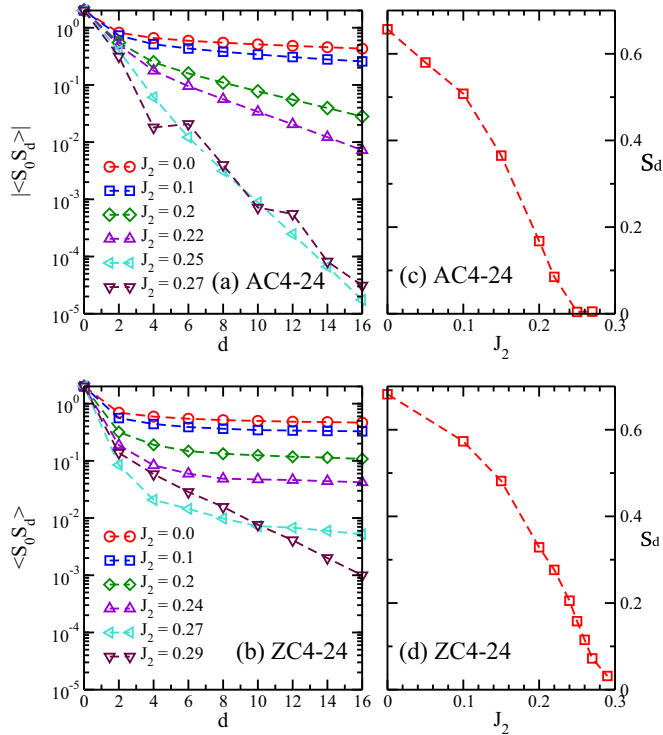
FIG. 4. (Color online) (a) and (b) are the log-linear plots of spin correlations on the AC4-24 and ZC4-24 cylinders. (c) and (d) are the J_2 dependence of the long-distance spin correlations $S_d \equiv \sqrt{|\langle S_0 S_d \rangle|}$ [d is the longest distance in (a) and (b)]. In subfigure (a), the correlation data for $J_2 < 0.27$ are all positive. For $J_2 = 0.27$, the Néel AFM pattern is destroyed, thus the correlations change sign in some places.

$J_2 \simeq 0.26$–0.28. We have also checked the spin correlations on the AC6 and ZC6 cylinders. Although the long-range correlations on these wider cylinders are not fully converged, their behaviors are qualitatively consistent with those on the AC4 and ZC4 cylinders.

III. STRIPE AFM PHASE

In the spin-1/2 J_1-J_2 honeycomb Heisenberg model, the system is in a staggered dimer phase with breaking lattice rotational symmetry and short-range spin correlations for $J_2 \gtrsim 0.35$. Interestingly, in this spin-1 system we find magnetically ordered states instead of the staggered dimer. As shown in Fig. 5(a) for $J_2 = 0.4$ on the AC6-18 cylinder, we find a magnetic ordered state with the eight-site unit cell denoted by the green dashed rectangle. This state is stable on all the AC cylinders that we have studied (AC4, AC6, and AC8). However, on the ZC6-18 cylinder at $J_2 = 0.4$, we find a stripe AFM state as shown in Fig. 5(b). This stripe state is also stable on the different ZC cylinders (ZC4, ZC6, and ZC8). In Figs. 6(a) and 6(b) of the log-linear plots of spin correlation functions at the large J_2 side, we find that the spin correlation length diminishes with decreasing J_2. On the AC4 cylinder, the spin correlations have a sharp increase for $J_2 \gtrsim 0.35$; and on the ZC4 cylinder, correlations grow rapidly for $J_2 \gtrsim 0.32$.

(a) J₂=0.4, AC6-18, left half lattice
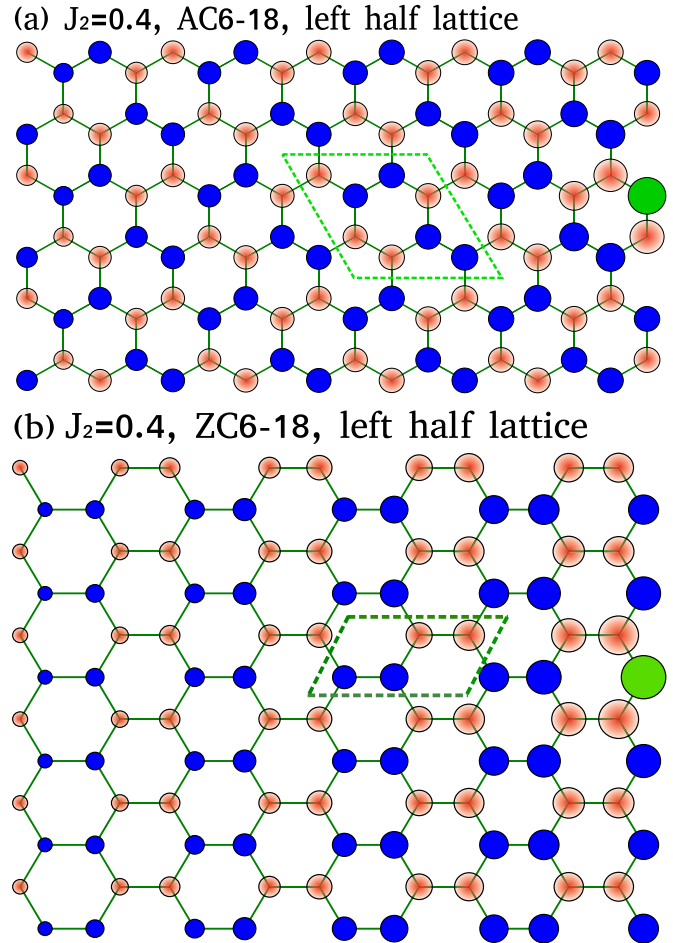

(b) J₂=0.4, ZC6-18, left half lattice

FIG. 5. (Color online) Spin correlation function $\langle \vec{S}_0 \cdot \vec{S}_j \rangle$ in real space for $J_2 = 0.4$ on the (a) AC6-18 cylinder and (b) ZC6-18 cylinder. The green site is the reference spin $\vec{S}_0$ in the middle of the lattice, and the blue solid and red shaded circles denote the positive and negative spin correlations, respectively. The area of the circle is proportional to the amplitude of correlations. The dashed rectangles denote the unit cells.

For $J_2 \lesssim 0.32$, the spin correlations decay quite fast to vanish, which is consistent with a nonmagnetic phase region.

To identify which state is the exact ground state at large J_2 side, we compare the ground-state energy on both cylinder geometries as shown in Fig. 6(c) for $J_2 = 0.4$. We extract the ground-state energy from the bulk bond energy on long cylinder systems. Interestingly, we find that the energies on ZC cylinders are always lower than those on AC cylinders. As we expect, the two geometries should give the same energy in the thermodynamic limit. Thus, the different energy in Fig. 6(c) indicates the strong finite-size effects on systems we can study. Although we cannot definitely determine which geometry gives the correct ground state in the thermodynamic limit, based on our calculations we believe that the stripe state on ZC cylinders would win because it always has the lower energy for system sizes we studied.

As shown in Fig. 1 of the spin configuration in the stripe AFM phase, we expect that the nearest-neighbor bond energies $\langle \vec{S}_i \cdot \vec{S}_j \rangle$ of the two parallel spins are positive and those between
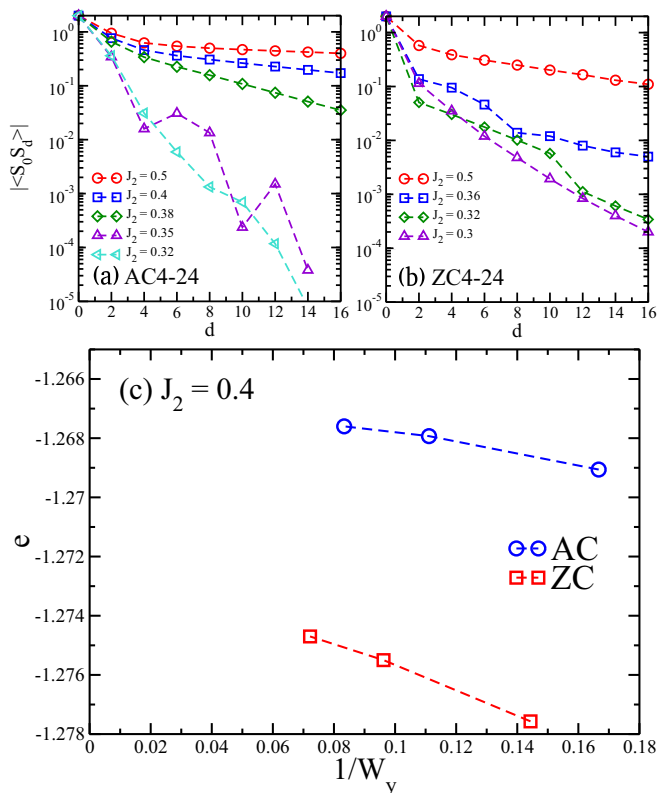
FIG. 6. (Color online) Log-linear plots of spin correlations at large J_2 side for the (a) AC4-24 and (b) ZC4-24 cylinders. (c) Cylinder width dependence of the bulk ground-state energy for $J_2 = 0.4$ on the AC and ZC cylinders. ZC cylinders always have a lower energy than AC cylinders.

the antiparallel spins are negative. This feature also can be used to characterize the appearance of the stripe phase. In Fig. 7, we demonstrate the bond energy for $J_2 = 0.5$ on the ZC4-24 cylinder, which indeed has the bond energy pattern expected for the stripe AFM phase. With decreasing J_2, we find that this bond energy pattern could persist to $J_2 = 0.32$, which is consistent with the phase transition point estimated from spin correlation function.
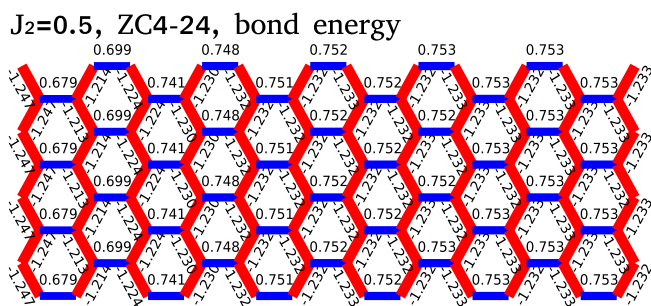

FIG. 7. (Color online) The nearest-neighbor bond energy for $J_2 = 0.5$ on the ZC4-24 cylinder. Here, we only show the left half lattice. The positive horizontal (labeled by blue) and the negative vertical (labeled by red) bond energies are consistent with the spin configuration in the stripe AFM state.

IV. INTERMEDIATE PHASE REGION

Next, we investigate the intermediate region between the two magnetic ordered phases. First of all, we calculate the first-neighbor bond energy $\langle S_i \cdot S_j \rangle$ to study the possible lattice symmetry breaking. To accommodate the possible valence-bond solid states on a cylinder system, we perform calculations on two cylinder geometries, the AC cylinder and the trimmed ZC (tZC) cylinder with some trimmed sites on the open boundaries [see the lattice in Fig. 8(b)] [40,41]. On the AC4 and tZC4 cylinders, the bond energies are quite uniform in the bulk of the cylinder, which is consistent with the short order correlation length on the narrow system. Thus, to detect the possible lattice symmetry breaking, we need to go to the wider systems to study the behavior of correlation length with growing cylinder width [40–42]. As the DMRG convergence in the intermediate region is quite challenging on the wider systems, we can only study the AC6 and tZC6 cylinders. During the DMRG calculations, we measure the bond energy by increasing the optimal state number step by step. By keeping the states up to 8000 $SU(2)$ states, we find a PVB dimer pattern stabilized as shown in Fig. 8, which is robust in the whole lattice and thus has broken the lattice translation symmetry on the finite-size cylinders. For the calculations on the AC6 and tZC6 cylinders by keeping 8000 states, the truncation errors are about 1×10^{-5}. Although we cannot obtain the more accurate results, based on the clearer PVB pattern with growing kept state number, we argue that the PVB order is stable on these geometries. Interestingly, the field-theory analyses have indicated that such a PVB state could emerge proximate to the Néel AFM phase on both the spin-1/2 and the spin-1 honeycomb Heisenberg models [72]. We also study the bond energy for other J_2 around the intermediate region. For $J_2 = 0.31$, the systems also exhibit the PVB pattern. However, for $J_2 \geqslant 0.32$ the bond energy pattern appears like in Fig. 7, consistent with the stripe state.

To further distinguish the three different phases, we calculate the spin gap on the long cylinder. As for the broken $SU(2)$ symmetry and emerging Goldstone boson, the spin gap is expected to vanish in both the Néel AFM and the stripe AFM phases. However, as for the spin singlet bonds formed in the valence-bond solid states, the spin gap should be nonzero in a PVB state. To find the spin gap on the cylinder, we follow the standard method in DMRG calculations. We first sweep a long cylinder to find the ground state with the energy E_0, and then we sweep the bulk by targeting the total spin $S = 1$ sector to find the lowest-energy state with the energy E_1. Then the spin gap of the bulk Δ_T is the difference between E_0 and E_1, $\Delta_T = E_1 - E_0$. We calculate the long cylinder to make sure the spin gap Δ_T is converged and independent of cylinder length. We do not show the data on AC cylinders as their ground state in the large J_2 side has a higher energy on our studied systems. As shown in Fig. 9(a), the spin gap Δ_T is vanishing small for $J_2 \lesssim 0.25$, which is consistent with the Néel AFM order. At $J_2 \simeq 0.27$, the spin gap increases dramatically and then decreases for $J_2 \gtrsim 0.35$. The enhanced spin gap in the intermediate region could be served as evidence for the valence-bond solid states. In the stripe phase $J_2 \gtrsim 0.32$, the spin gap is large on the ZC4 cylinder, which is related to finite-size effects because it should be vanished in the
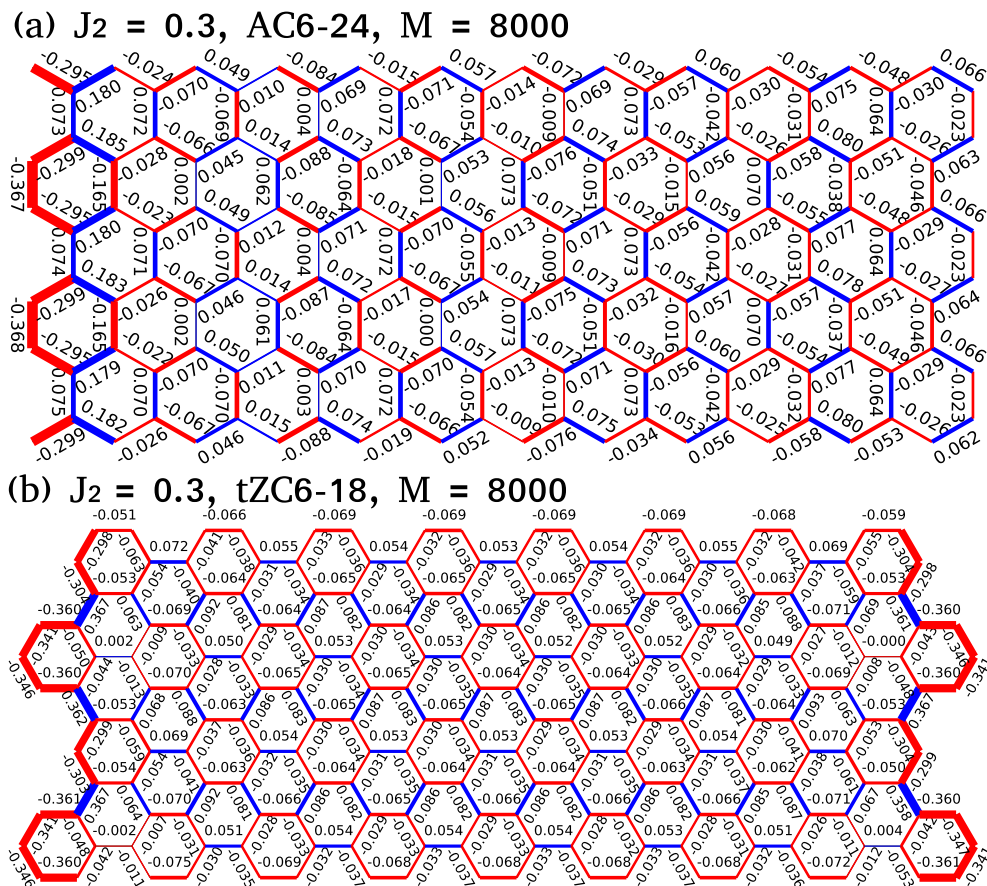
FIG. 8. (Color online) The nearest-neighbor bond energy textures for $J_2 = 0.3$ on the (a) AC6-24 cylinder and (b) tZC6-18 cylinder, which are obtained by keeping 8000 $SU(2)$ states. The bond textures are obtained by subtracting the average bond energy. The blue and red bonds denote the positive and negative bond textures, respectively. On both geometries, a PVB bond pattern is found. For AC6-24 in (a), only the left half lattice is shown here.

thermodynamic limit. This size effect can be understood from the bond energy in Fig. 7, which has the AFM bonds along the y axis. Thus, the spin triplet gap is strongly correlated with the size scale in the y direction, which accounts for the large gap on the narrow ZC4 cylinder. To show the size dependence of spin gap on the cylinder width, we also calculate the spin gap

FIG. 9. (Color online) (a) J_2 dependence of the spin gap on the ZC4 and ZC6 cylinder systems. (b) Cylinder width dependence of the bulk ground-state energy on AC (AC4 and AC6) and ZC (ZC4 and ZC6) cylinders for $J_2 = 0.3$.

on the ZC6 cylinder deep inside the stripe phase. As expected, the spin gap on the ZC6 cylinder drops rapidly, consistent with the vanished gap in the thermodynamic limit. We do not show the spin gap on the ZC6 cylinder for the intermediate region because the DMRG calculations in the spin-1 sector are quite far from convergence in this region.

Finally, we demonstrate the bulk ground-state energy for $J_2 = 0.3$ on different cylinders. We obtain the bulk energy from calculating all the bond energy in the middle of the cylinder. As shown in Fig. 9(b), the ground-state energy at $J_2 = 0.3$ smoothly increases with growing cylinder width, which behaves differently from the energy scaling in the stripe phase demonstrated in Fig. 6(c), where the energies on the two geometries scale separately. We also notice that the ground-state energy per site at $J_2 = 0.3$ changes slightly with growing system width. The energy appears to approach $e_\infty \simeq -1.262$, which provides an upper bound for the ground-state energy in the thermodynamic limit.
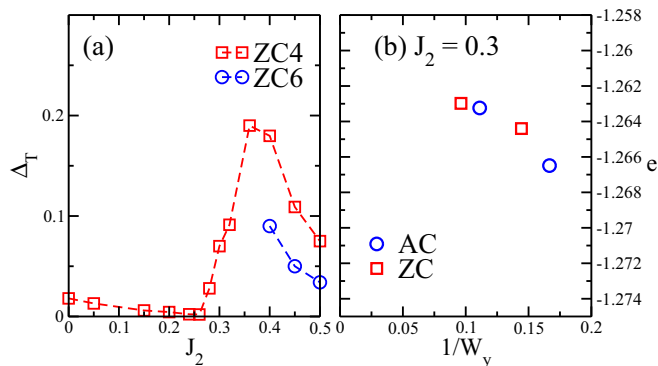
V. ENTANGLEMENT ENTROPY AND SPECTRUM

To further characterize the different phases and phase transitions, we study the bipartite entanglement entropy and entanglement spectrum. In Fig. 10(a), we demonstrate the J_2 dependence of entropy on the ZC4 cylinder. The entropy shows
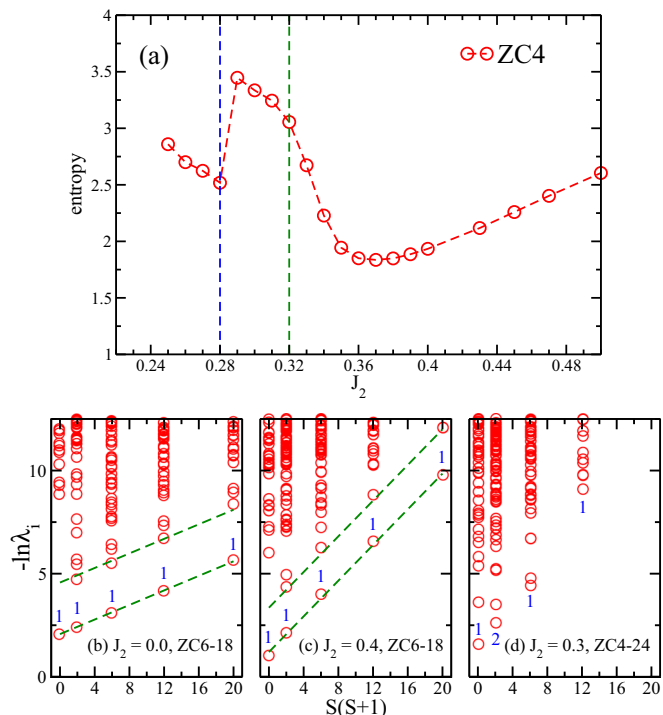
FIG. 10. (Color online) (a) J_2 dependence of the bipartite entanglement entropy on the ZC4 cylinder. At $J_2 \simeq 0.28$ and 0.32, the entropy has the sharp jump and drop, which appear consistent with the quantum phase transitions. Entanglement spectra for (b) $J_2 = 0.0$ on the ZC6-18 cylinder, (c) $J_2 = 0.4$ on the ZC6-18 cylinder, and (d) $J_2 = 0.3$ on the ZC4-24 cylinder. The blue numbers denote the number of the largest eigenvalues in each S sector. The green dashed lines denote the tower of states structure in the magnetic ordered states.

a sharp jump at $J_2 \simeq 0.28$ and a drop at $J_2 \simeq 0.32$, which have been shown to characterize various phase transitions in one-dimensional systems [73–76] and are consistent with the identified transition points. While the discontinuous jump at $J_2 \simeq 0.28$ suggests a first-order transition from the Néel AFM to the nonmagnetic phase, the smoother entropy decrease near $J_2 \simeq 0.32$ might be consistent with a weak first-order transition.

In Figs. 10(b)–10(d), we demonstrate the bipartite entanglement spectrum in each phase. For the ordered phases with continuous symmetry breaking, the lower part of the entanglement spectrum is in correspondence with the "tower of states" (TOS) spectrum [77–79]. In Figs. 10(b) and 10(c) of the spectra in both the magnetic ordered states with breaking $SU(2)$ to $U(1)$ symmetry, the spectra have a single dominant eigenvalue in each S sector, which are separated from the

higher levels by the entanglement gap and follow a linear behavior with $S(S + 1)$ (S is the quantum number of total spin). All these features are consistent with the TOS structures of the energy spectra in the corresponding magnetic ordered states on the honeycomb lattice [55]. In the intermediate phase region, the spectrum is totally different from the magnetic ordered states, as shown in Fig. 10(d) for $J_2 = 0.3$ on the ZC4 cylinder [80]. The low-lying degeneracy in the $S = 1$ sector changes from 1 to 2, and there is no clear entanglement gap between the largest eigenvalues and the rest of the spectrum. These features distinguish the intermediate phase from the magnetic ordered phases.

VI. SUMMARY

We have studied the quantum phase diagram of the spin-1 J_1-J_2 Heisenberg model on the honeycomb lattice using density-matrix renormalization group calculations on the cylinder system. We have established three different phases including two magnetic ordered phases and a nonmagnetic phase. For $J_2 \lesssim 0.27$, we find a Néel AFM phase. For $J_2 \gtrsim 0.32$, we find two possible candidate magnetic ordered states depending on the different geometries. On AC cylinders, the system is a magnetic order state with the eight-site unit cell, while on ZC cylinders it is a stripe AFM state. By comparing the bulk ground-state energy on the two geometries, we find that the ZC cylinders always have a lower energy than the AC cylinders, which strongly suggests the stripe AFM state as the true ground state in the thermodynamic limit.

Between these two magnetically ordered phases with $0.27 \lesssim J_2 \lesssim 0.32$, we find a nonmagnetic phase region. On both the 6 and tZC6 cylinders, the systems have nonuniform bond energy. By increasing the kept states to 8000 $SU(2)$ states [equivalent to about 24 000 $U(1)$ states], we find a stable plaquette valence-bond order emerging in the systems. The spin gap on finite-size cylinder also enhances dramatically in this phase region. Our results indicate that the plaquette state is a strong candidate for this nonmagnetic phase. Moreover, the sizable entropy change on the phase boundaries indicates that the nature of the phase transitions from the magnetic ordered phases to the nonmagnetic phase might be first order.

[1] P. W. Anderson, Mater. Res. Bull. **8**, 153 (1973).

[2] D. S. Rokhsar and S. A. Kivelson, Phys. Rev. Lett. **61**, 2376 (1988).

[3] L. Balents, Nature (London) **464**, 199 (2010).

[4] R. Moessner and S. L. Sondhi, Phys. Rev. Lett. **86**, 1881 (2001).

[5] C. Nayak and K. Shtengel, Phys. Rev. B **64**, 064422 (2001).

[6] T. Senthil and O. Motrunich, Phys. Rev. B **66**, 205104 (2002).

[7] L. Balents, M. P. A. Fisher, and S. M. Girvin, Phys. Rev. B **65**, 224412 (2002).

[8] D. N. Sheng and L. Balents, Phys. Rev. Lett. **94**, 146805 (2005).

[9] A. Kitaev, Ann. Phys. (NY) **321**, 2 (2006).

[10] H. Yao and S. A. Kivelson, Phys. Rev. Lett. **99**, 247203 (2007).

[11] S. V. Isakov, M. B. Hastings, and R. G. Melko, Nat. Phys. **7**, 772 (2011).

[12] P. A. Lee, N. Nagaosa, and X.-G. Wen, Rev. Mod. Phys. **78**, 17 (2006).

[13] P. A. Lee, Science **321**, 1306 (2008).

[14] P. Mendels, F. Bert, M. A. de Vries, A. Olariu, A. Harrison, F. Duc, J. C. Trombe, J. S. Lord, A. Amato, and C. Baines, Phys. Rev. Lett. **98**, 077204 (2007).

[15] J. S. Helton, K. Matan, M. P. Shores, E. A. Nytko, B. M. Bartlett, Y. Yoshida, Y. Takano, A. Suslov, Y. Qiu, J.-H. Chung *et al.*, Phys. Rev. Lett. **98**, 107204 (2007).

[16] M. A. de Vries, J. R. Stewart, P. P. Deen, J. O. Piatek, G. J. Nilsen, H. M. Rønnow, and A. Harrison, Phys. Rev. Lett. **103**, 237201 (2009).

[17] T.-H. Han, J. S. Helton, S. Chu, D. G. Nocera, J. A. Rodriguez-Rivera, C. Broholm, and Y. S. Lee, Nature (London) **492**, 406 (2012).

[18] R. Colman, C. Ritter, and A. Wills, Chem. Mater. **20**, 6897 (2008).

[19] B. Fåk, E. Kermarrec, L. Messio, B. Bernu, C. Lhuillier, F. Bert, P. Mendels, B. Koteswararao, F. Bouquet, J. Ollivier *et al.*, Phys. Rev. Lett. **109**, 037208 (2012).

[20] B. Bernu, C. Lhuillier, E. Kermarrec, F. Bert, P. Mendels, R. H. Colman, and A. S. Wills, Phys. Rev. B **87**, 155107 (2013).

[21] E. Kermarrec, A. Zorko, F. Bert, R. H. Colman, B. Koteswararao, F. Bouquet, P. Bonville, A. Hillier, A. Amato, J. van Tol *et al.*, Phys. Rev. B **90**, 205103 (2014).

[22] H. C. Jiang, Z. Y. Weng, and D. N. Sheng, Phys. Rev. Lett. **101**, 117203 (2008).

[23] S. Yan, D. A. Huse, and S. R. White, Science **332**, 1173 (2011).

[24] S. Depenbrock, I. P. McCulloch, and U. Schollwöck, Phys. Rev. Lett. **109**, 067201 (2012).

[25] H.-C. Jiang, Z. Wang, and L. Balents, Nat. Phys. **8**, 902 (2012).

[26] Y. Ran, M. Hermele, P. A. Lee, and X.-G. Wen, Phys. Rev. Lett. **98**, 117205 (2007).

[27] Y. Iqbal, F. Becca, S. Sorella, and D. Poilblanc, Phys. Rev. B **87**, 060405 (2013).

[28] Y. Iqbal, D. Poilblanc, and F. Becca, Phys. Rev. B **89**, 020407 (2014).

[29] L. Messio, B. Bernu, and C. Lhuillier, Phys. Rev. Lett. **108**, 207204 (2012).

[30] S.-S. Gong, W. Zhu, and D. N. Sheng, Sci. Rep. **4**, 6317 (2014).

[31] Y.-C. He, D. N. Sheng, and Y. Chen, Phys. Rev. Lett. **112**, 137202 (2014).

[32] B. Bauer, L. Cincio, B. P. Keller, M. Dolfi, G. Vidal, S. Trebst, and A. W. W. Ludwig, Nat. Commun. **5**, 5137 (2014).

[33] B. K. Clark, D. A. Abanin, and S. L. Sondhi, Phys. Rev. Lett. **107**, 087204 (2011).

[34] Y.-M. Lu and Y. Ran, Phys. Rev. B **84**, 024420 (2011).

[35] F. Wang, Phys. Rev. B **82**, 024419 (2010).

[36] H.-C. Jiang, H. Yao, and L. Balents, Phys. Rev. B **86**, 024424 (2012).

[37] W.-J. Hu, F. Becca, A. Parola, and S. Sorella, Phys. Rev. B **88**, 060402 (2013).

[38] L. Wang, D. Poilblanc, Z.-C. Gu, X.-G. Wen, and F. Verstraete, Phys. Rev. Lett. **111**, 037202 (2013).

[39] R. Ganesh, J. van den Brink, and S. Nishimoto, Phys. Rev. Lett. **110**, 127203 (2013).

[40] Z. Zhu, D. A. Huse, and S. R. White, Phys. Rev. Lett. **110**, 127205 (2013).

[41] S.-S. Gong, D. N. Sheng, O. I. Motrunich, and M. P. A. Fisher, Phys. Rev. B **88**, 165138 (2013).

[42] S.-S. Gong, W. Zhu, D. N. Sheng, O. I. Motrunich, and M. P. A. Fisher, Phys. Rev. Lett. **113**, 027201 (2014).

[43] Q. Si and E. Abrahams, Phys. Rev. Lett. **101**, 076401 (2008).

[44] C. Fang, H. Yao, W.-F. Tsai, J. P. Hu, and S. A. Kivelson, Phys. Rev. B **77**, 224509 (2008).

[45] C. Xu, M. Müller, and S. Sachdev, Phy. Rev. B **78**, 020501 (2008).

[46] H. C. Jiang, F. Krüger, J. E. Moore, D. N. Sheng, J. Zaanen, and Z. Y. Weng, Phys. Rev. B **79**, 174409 (2009).

[47] R. Yu, Z. Wang, P. Goswami, A. H. Nevidomskyy, Q. Si, and E. Abrahams, Phys. Rev. B **86**, 085148 (2012).

[48] R. Yu and Q. Si, Phys. Rev. Lett. **115**, 116401 (2015).

[49] F. Wang, S. A. Kivelson, and D.-H. Lee, Nat. Phys. **11**, 959 (2015).

[50] Y. Nishikubo, K. Kudo, and M. Nohara, J. Phys. Soc. Jpn. **80**, 055002 (2011).

[51] S. J. Youn, M. H. Fischer, S. H. Rhim, M. Sigrist, and D. F. Agterberg, Phys. Rev. B **85**, 220505 (2012).

[52] J. Goryo, M. H. Fischer, and M. Sigrist, Phys. Rev. B **86**, 100507 (2012).

[53] P. K. Biswas, H. Luetkens, T. Neupert, T. Stürzer, C. Baines, G. Pascua, A. P. Schnyder, M. H. Fischer, J. Goryo, M. R. Lees *et al.*, Phys. Rev. B **87**, 180503 (2013).

[54] M. H. Fischer, T. Neupert, C. Platt, A. P. Schnyder, W. Hanke, J. Goryo, R. Thomale, and M. Sigrist, Phys. Rev. B **89**, 020509 (2014).

[55] J. Fouet, P. Sindzingre, and C. Lhuillier, Eur. Phys. J. B **20**, 241 (2001).

[56] H. Mosadeq, F. Shahbazi, and S. Jafari, J. Phys.: Condens. Matter **23**, 226006 (2011).

[57] A. F. Albuquerque, D. Schwandt, B. Hetényi, S. Capponi, M. Mambrini, and A. M. Läuchli, Phys. Rev. B **84**, 024406 (2011).

[58] A. Mulder, R. Ganesh, L. Capriotti, and A. Paramekanti, Phys. Rev. B **81**, 214419 (2010).

[59] D. C. Cabra, C. A. Lamas, and H. D. Rosales, Phys. Rev. B **83**, 094506 (2011).

[60] H. Zhang and C. A. Lamas, Phys. Rev. B **87**, 024415 (2013).

[61] C. Xu and L. Balents, Phys. Rev. B **84**, 014402 (2011).

[62] J. Reuther, D. A. Abanin, and R. Thomale, Phys. Rev. B **84**, 014417 (2011).

[63] J. Oitmaa and R. R. P. Singh, Phys. Rev. B **84**, 094424 (2011).

[64] F. Mezzacapo and M. Boninsegni, Phys. Rev. B **85**, 060402 (2012).

[65] R. Bishop, P. Li, D. Farnell, and C. Campbell, J. Phys.: Condens. Matter **24**, 236002 (2012).

[66] H. D. Rosales, D. C. Cabra, C. A. Lamas, P. Pujol, and M. E. Zhitomirsky, Phys. Rev. B **87**, 104402 (2013).

[67] R. Flint and P. A. Lee, Phys. Rev. Lett. **111**, 217201 (2013).

[68] A. Di Ciolo, J. Carrasquilla, F. Becca, M. Rigol, and V. Galitski, Phys. Rev. B **89**, 094413 (2014).

[69] L. Messio, C. Lhuillier, and G. Misguich, Phys. Rev. B **83**, 184401 (2011).

[70] S. R. White, Phys. Rev. Lett. **69**, 2863 (1992).

[71] I. P. McCulloch and M. Gulácsi, Eur. Phys. Lett. **57**, 852 (2002).

[72] N. Read and S. Sachdev, Phys. Rev. B **42**, 4568 (1990).

[73] Y. Chen, P. Zanardi, Z. Wang, and F. Zhang, New J. Phys. **8**, 97 (2006).

[74] S.-S. Deng, S.-J. Gu, and H.-Q. Lin, Phys. Rev. B **74**, 045103 (2006).

[75] M. Kargarian, R. Jafari, and A. Langari, Phys. Rev. A **77**, 032346 (2008).

[76] G.-H. Liu, W. Li, W.-L. You, G.-S. Tian, and G. Su, Phys. Rev. B **85**, 184422 (2012).

[77] M. A. Metlitski and T. Grover, arXiv:1112.5166.

[78] V. Alba, M. Haque, and A. M. Läuchli, Phys. Rev. Lett. **110**, 260403 (2013).

[79] F. Kolley, S. Depenbrock, I. P. McCulloch, U. Schollwöck, and V. Alba, Phys. Rev. B **88**, 144426 (2013).

[80] We do not show the entanglement spectrum for the ZC6 cylinder because compared with bond energy, it is harder to obtain the converged entanglement spectrum on the ZC6 cylinder.